

## Topological Edge State in the Two-Dimensional Stampfli-Triangle Photonic Crystals

Bei Yan, Jianlan Xie, Exian Liu, Yuchen Peng, Rui Ge, Jianjun Liu<sup>✉</sup>,\* and Shuangchun Wen  
*Key Laboratory for Micro/Nano Optoelectronic Devices of Ministry of Education & Hunan Provincial Key Laboratory of Low-Dimensional Structural Physics and Devices, School of Physics and Electronics, Hunan University, Changsha 410082, China*

 (Received 14 January 2019; revised manuscript received 16 August 2019; published 2 October 2019)

A two-dimensional Stampfli-triangle photonic crystal (2D S-T PC), which arranges the basic structural unit of a Stampfli-type photonic quasicrystal (PQC) in a triangular lattice, is proposed. The relationship between the structural parameters and the topological trivial or nontrivial state generated in the 2D S-T PC and the relationship between the structural parameters and the frequency of the one-way propagation are analyzed. One-way propagation based on a U-shaped waveguide composed of 2D S-T PCs, with topological trivial and nontrivial states sharing a common band gap, is realized. The topological edge state, which satisfies  $C_6$  symmetry, is realized by changing just the diameters of the cylinders in the 2D S-T PC. This provides an idea for the generation of a topological edge state based on a 2D PQC and increases the diversity and adjustability of the method to realize the topological edge state.

DOI: [10.1103/PhysRevApplied.12.044004](https://doi.org/10.1103/PhysRevApplied.12.044004)

### I. INTRODUCTION

The photonic quantum Hall effect (PQHE) and its one-way propagation effect have been proved theoretically based on photonic crystals [1,2], which has opened the way for research on topological photonics. The topological edge state has set off a research boom due to its excellent topological properties, such as robustness, back-scattering suppression, and defect immunity (see, e.g., [3–7]). Under the applied external magnetic field, an imaginary part occurs in the nondiagonal term of the magnetic permeability tensor of the gyromagnetic material, which breaks the time-reversal symmetry of the system and realizes a stable topological edge state. However, based on the gyromagnetic [8–12] or gyroelectric [13] materials, the working frequency domain of the light source is limited to the microwave frequency. Weak magneto-optical effects in the optical-frequency range lead to a significant absorption loss, which limits the application of the PQHE at the most common optical frequencies.

To solve this problem, researchers use all-dielectric materials to achieve topological edge states that suit the optical frequency. These include Floquet topological insulators [14–18], valley Hall effects [19–22], and photonic quantum spin Hall effects (PQSHEs) [23–28]. The PQSHE generated by a photonic crystal with  $C_6$  symmetry has been extensively researched, including the honeycomb lattice of circle scatterers (dielectric cylinders [23,26,28] or air holes [27]) or triangular air holes [25] and the triangular lattice

of annular dielectric cylinders [24]. The PQSHE based on a photonic crystal with  $C_6$  symmetry has also been experimentally verified in the microwave frequency range [29]. In order to generate the topological edge state, the spacing of the cylinders in the primitive cell needs to be expanded or shrunken in the honeycomb lattice, or annular cylinders needs to be adopted and the inner and outer radii of the annular cylinders changed in the triangular lattice. The honeycomb lattice can be seen as a triangular lattice arranged using primitive cells that consist of complex hexagonal lattices and both the honeycomb lattice and the triangular lattice satisfy  $C_6$  symmetry. It can be conjectured that a triangular lattice arranged using primitive cells that satisfy  $C_6$  symmetry will generate a topological edge state. There will be more selectivity and adjustability for the primitive cell structure and a greater diversity of methods for generating topological edge states. The Stampfli-type PQC, which has been extensively researched, satisfies  $C_6$  symmetry [30] and can be applied to band-gap devices [31], lasers [32,33], negative-refraction imaging [34,35], the zero-refraction index [36], fibers [37–40], and other fields. Moreover, 2D PQC structures can generate topological edge states with rich band structures and topological band gaps [41].

In this paper, the basic structural unit of the Stampfli-type PQC is used as the primitive cell and arranged into a triangular lattice to form a 2D S-T PC. A topological edge state can be generated and the PQSHE can be realized by changing just the diameters of the cylinders, instead of expanding or shrinking the space occupied by the cylinders or adopting annular cylinders in the primitive cell.

\*jianjun.liu@hnu.edu.cn

## II. MODELS AND THEORY

The structure of the proposed 2D S-T PC is shown in Fig. 1. As shown in Fig. 1(a), the combination structure of an equilateral triangle and a square is rotated six times around a vertex of the equilateral triangle and cylinders are arranged at each vertex to obtain the basic structural unit of the Stampfli-type PQC [30–32,34]. This structure rotates  $60^\circ$  around its center along the angular phase and coincides with itself, i.e., this structure satisfies  $C_6$  symmetry. The basic structural unit of the Stampfli-type PQC is used as the primitive cell and is arranged in a triangular lattice to form the 2D S-T PC. The lattice constant is  $a$ , the cylinders in the primitive cell are silicon (relative dielectric constant  $\epsilon_{RD} = 11.7$ ), and the background material is air ( $\epsilon_{RA} = 1$ ). The distance between the cylinders in the primitive cell  $R = a/(3 + \sqrt{3})$ . The cylinders are divided into two categories: one category includes seven cylinders of diameter  $d_1$  in the inner ring and the center and the other category includes twelve cylinders of diameter  $d_2$  in the outer ring—2D S-T PCs with different diameters  $d_1$  and  $d_2$  are shown in Figs. 1(a) and 1(b), respectively.

A system satisfying  $C_6$  symmetry can realize the PQSHE, which can be proved by  $\mathbf{k} \cdot \mathbf{P}$  theory [23,24,42, 43]. The detailed theoretical derivation, taken from Ref. [24], is as follows. In transverse-magnetic (TM) mode, the Maxwell equations can be abbreviated as follows:

$$\nabla \times \frac{1}{\epsilon(\mathbf{r})} \nabla \times \mathbf{h}_{n,\mathbf{k}}(\mathbf{r}) = \frac{\omega^2}{c^2} \mathbf{h}_{n,\mathbf{k}}(\mathbf{r}), \quad (1)$$

where  $n$  represents the photonic band index,  $\mathbf{h}_{n,\mathbf{k}}(\mathbf{r})$  represents the Bloch function of the magnetic field and its normalized expression is as follows:

$$\int_{\text{u.c.}} d\mathbf{r} \cdot \mathbf{h}_{n',\mathbf{k}}^* \cdot \mathbf{h}_{n,\mathbf{k}}(\mathbf{r}) = \delta_{nn'}, \quad (2)$$

where the integral region u.c. represents a primitive cell. Expanding the Bloch function  $\mathbf{h}_{n,\mathbf{k}}(\mathbf{r})$  at the  $\Gamma$  point, the

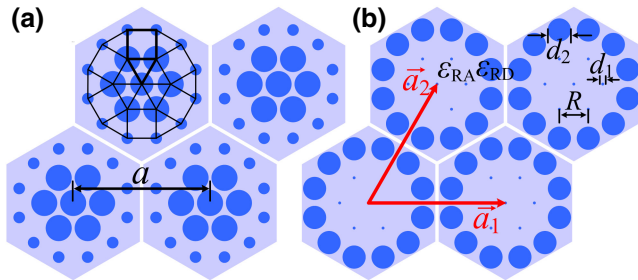


FIG. 1. The 2D S-T PC: (a)  $d_1 = 0.9R$ ,  $d_2 = 0.4R$ ; (b)  $d_1 = 0.1R$ ,  $d_2 = 0.8R$ .

$\mathbf{k} \cdot \mathbf{P}$  Hamiltonian of the system can be obtained as follows:

$$H_{nn'} = \frac{\omega_{n,0}^2}{c^2} \delta_{nn'} + \mathbf{k} \cdot \mathbf{P}_{nn'} - \int_{\text{u.c.}} \frac{d\mathbf{r}}{\epsilon(\mathbf{r})} \mathbf{h}_{n,0}^* \cdot [\mathbf{k} \times (\mathbf{k} \times \mathbf{h}_{n',0}(\mathbf{r}))], \quad (3)$$

where  $\omega_{n,0}$  represents the eigenfrequency of the  $n$ th band at the  $\Gamma$  point and  $\mathbf{P}$  represents momentum, with its matrix element being shown as follows:

$$\mathbf{P}_{nn'}(\mathbf{k}) = \int_{\text{u.c.}} \frac{d\mathbf{r}}{\epsilon(\mathbf{r})} [\mathbf{h}_{n,0}^*(\mathbf{r}) \times (i\nabla \times \mathbf{h}_{n',0}(\mathbf{r})) + (i\nabla \times \mathbf{h}_{n',0}(\mathbf{r})) \times \mathbf{h}_{n,0}^*(\mathbf{r})]. \quad (4)$$

From Eqs. (3) and (4), it can be seen that the matrix element of momentum  $\mathbf{P}$  is nonzero only when the parities of the  $n$  and  $n'$  bands are different. The parities of the two bands of the 2D S-T PC are called the  $p$  band and the  $d$  band which are illustrated in Fig. 4, respectively. Thus, the effective Hamiltonian under the basis of  $(p_+, d_+, p_-, d_-)^T$  can be deduced as follows:

$$H = \begin{pmatrix} \frac{\omega_p^2}{c^2} & Ak_+ & 0 & 0 \\ A^*k_- & \frac{\omega_d^2}{c^2} & 0 & 0 \\ 0 & 0 & \frac{\omega_p^2}{c^2} & A^*k_- \\ 0 & 0 & Ak_+ & \frac{\omega_d^2}{c^2} \end{pmatrix}, \quad (5)$$

where  $k_{\pm} = k_x \pm ik_y$ ,  $A$  represents the coupling coefficient between different states, and  $\omega_p$  and  $\omega_d$ , respectively, represent the frequency of the  $p$  band and  $d$  band at the  $\Gamma$  point. Equation (5) indicates that only  $p_+, d_+$  states (or  $p_-, d_-$  states) with the same pseudospin can be coupled. In Eq. (5), the two square submatrices on the diagonal correspond to the Dirac equations containing the mass terms of pseudospin up and pseudospin down, respectively. The pseudospin photonic pairs are connected by the operation of time-reversal symmetry, which ensures that the whole system still protects time-reversal symmetry. Therefore, if the  $p$  band is regarded as the valence band and the  $d$  band is regarded as the conduction band, by analogy with the model used in the electronic system, the PQSHE can be described by Eq. (5). When  $\omega_p < \omega_d$ , the system generates a topological trivial state. When  $\omega_p > \omega_d$ , a  $p$ - $d$  parity inversion occurs at the  $\Gamma$  point, which will lead directly to the topological nontrivial state for photons. When the 2D S-T PCs with topological trivial and nontrivial states share a common band gap, a topological edge state will be generated at the interface of the two 2D S-T PCs and light with a frequency at the topological edge state can realize one-way propagation.

In order to determine the relationship between the structural parameters and the topological trivial or nontrivial

state generated in the 2D S-T PC, the variable  $\omega_{pd}$  is introduced as follows:

$$\omega_{pd} = \frac{2(\omega_d - \omega_p)}{\omega_d + \omega_p}, \quad (6)$$

where the structure with  $\omega_{pd} > 0$  generates the topological trivial state and the structure with  $\omega_{pd} < 0$  generates the topological nontrivial state. What needs to be demonstrated is that  $\omega_{pd}$  is not a band gap. As illustrated with the  $p$  and  $d$  bands and the frequency range marked as a gray area in Figs. 4(a) and 4(c), the value of  $\omega_{pd}$  is determined by  $\omega_p$  and  $\omega_d$ , which are set out in Eq. (5), while the frequency range of the band gap is from the highest frequency of the lower band to the lowest frequency of the upper band.

### III. RESULTS AND DISCUSSION

Topological trivial and nontrivial states can be generated by shrinking and expanding the honeycomb lattice, respectively [23,26,28,29]. The method to generate topological trivial and nontrivial states based on the 2D S-T PC can be analogously derived from the honeycomb lattice as shown in Fig. 2.

After shrinking [Fig. 2(c)] and expanding [Fig. 2(d)] the honeycomb lattice [Fig. 2(b)], the topological trivial state ( $\omega_{pd} > 0$ ) and the topological nontrivial state ( $\omega_{pd} < 0$ ) can be obtained, respectively. The structures in Figs. 2(e) and 2(f) can be obtained by deformation from the shrinking and expanding honeycomb lattice, respectively. According to Fig. 2(a), as  $d_1$  ( $d_2$ ) increases, the value of  $\omega_{pd}$  in the 2D S-T PC with the primitive cell structure as shown in Figs. 2(e) or 2(g) [2(f) or 2(h)] increases (decreases) gradually and the value is always greater (less) than zero, i.e., the characteristic of this 2D S-T PC is consistent with that of the shrunken (expanding) honeycomb lattice, which generates the topological trivial (nontrivial) state. The structures in Figs. 2(e) and 2(f) can be seen as the structure formed by the cylinders in the inner ring [Fig. 2(g)] and the outer ring [Fig. 2(h)] of a primitive cell structure of the 2D S-T PC, respectively. In other words, when combining the structures in Figs. 2(e) and 2(f), the primitive cell structure of the 2D S-T PC can be formed as shown in Fig. 2(i). It can be conjectured that 2D S-T PCs dominated by the inner-ring cylinders ( $d_2/d_1 < 1$ ) and the outer-ring cylinders ( $d_2/d_1 > 1$ ) can generate topological trivial and nontrivial states, respectively.

In order to further determine the relationship between the structural parameters and the topological trivial or nontrivial state generated in the 2D S-T PC, the values of  $\omega_{pd}$  and the band-gap distribution in the 2D S-T PC under different structural parameters are calculated, as shown in Fig. 3.

When  $d_1 = 0.4R$ ,  $0.5R$ , and  $0.6R$  and  $d_2/d_1$  changes from 0 to 2, the variation trend of  $\omega_{pd}$  in the 2D S-T PC

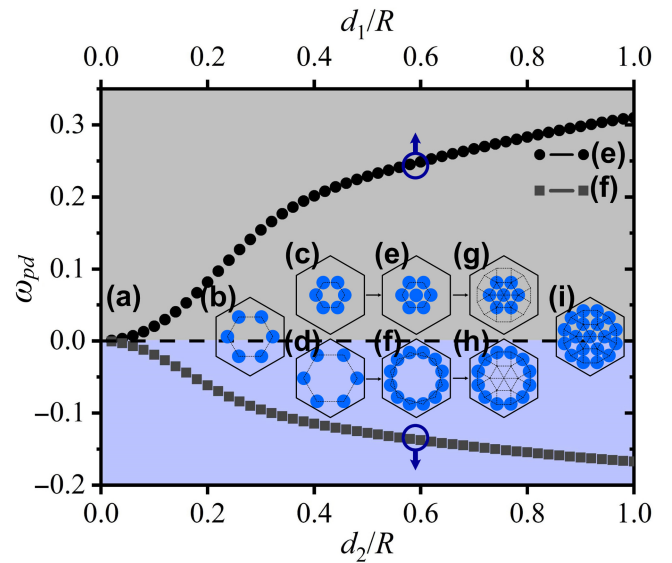


FIG. 2. (a) The variation trend of  $\omega_{pd}$  with changing  $d_1$  but  $d_2 = 0$ , and changing  $d_2$  but  $d_1 = 0$ , in the 2D S-T PC with the primitive cell structures shown in (e) or (g) and (f) or (h). (b) The honeycomb lattice. (c) The shrunken honeycomb lattice. (d) The expanded honeycomb lattice. (e) The structure formed by adding a central cylinder to the shrunken honeycomb lattice. (f) A combination structure formed by rotating the expanded honeycomb lattice cylinders  $+\pi/12$  and  $-\pi/12$  around the center, respectively. (g) A primitive cell of a 2D S-T PC with  $d_2 = 0$  but  $d_1 \neq 0$ . (h) A primitive cell of a 2D S-T PC with  $d_1 = 0$  but  $d_2 \neq 0$ . (i) A primitive cell of a 2D S-T PC with  $d_1 = d_2 \neq 0$ .

is shown in Fig. 3(a). As  $d_2/d_1$  increases,  $\omega_{pd}$  decreases monotonically:  $\omega_{pd} > 0$  when  $d_2/d_1 < 1$ ,  $\omega_{pd} = 0$  when  $d_2/d_1 = 1$ , and  $\omega_{pd} < 0$  when  $d_2/d_1 > 1$ . In the case of different values of  $d_1$ , the curves in Fig. 3(a) are monotonically decreasing. It can be seen that the structure of  $d_2/d_1 < 1$  (the inner-ring cylinders play a leading role) generates the topological trivial state and the structure of  $d_2/d_1 > 1$  (the outer-ring cylinders play a leading role) generates the topological nontrivial state. Therefore, the structural parameters can be used to distinguish or adjust the generation of topological trivial and nontrivial states directly. As shown in Fig. 3(b), the band-gap frequency of a 2D S-T PC with a topological trivial state varies within the range of  $[0.443(a/\lambda), 0.786(a/\lambda)]$  when  $d_1$  and  $d_2$  change. As  $d_2$  increases with  $d_1$  taking an arbitrary value, the band-gap width and the band-gap center frequency gradually decrease. As  $d_1$  increases with  $d_2$  taking an arbitrary value, the band-gap width gradually increases and the band-gap center frequency gradually decreases. As shown in Fig. 3(c), the band-gap frequency of a 2D S-T PC with a topological nontrivial state varies within the range of  $[0.391(a/\lambda), 0.672(a/\lambda)]$  when  $d_1$  and  $d_2$  change. As  $d_1$  increases with  $d_2$  taking an arbitrary value, the band-gap width and the band-gap center frequency gradually

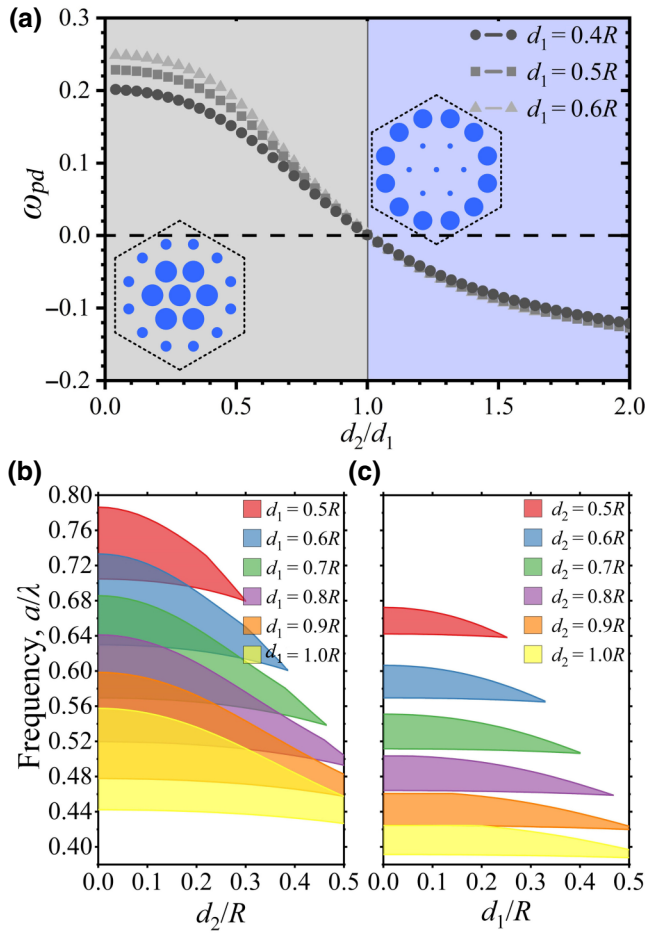


FIG. 3. (a) The variation trend of  $\omega_{pd}$  in the 2D S-T PC with changing  $d_2/d_1$  when  $d_1 = 0.4R$ ,  $0.5R$ , and  $0.6R$  respectively. The band-gap distribution diagram of 2D S-T PCs with topological trivial and nontrivial states when  $d_1$  and  $d_2$  change: (b) a 2D S-T PC with a topological trivial state, that is, the structure of  $d_2/d_1 < 1$ ; (c) a 2D S-T PC with a topological nontrivial state, that is, the structure of  $d_2/d_1 > 1$ .

decrease. As  $d_2$  increases with  $d_1$  taking an arbitrary value, the band-gap width gradually increases and the band-gap center frequency gradually decreases. Thereby, 2D S-T PCs with topological trivial and nontrivial states sharing a common band gap in the frequency range of  $[0.443(a/\lambda), 0.672(a/\lambda)]$  can be obtained from Figs. 3(b) and 3(c). Therefore, topological edge states in the frequency range of  $[0.443(a/\lambda), 0.672(a/\lambda)]$  can be achieved by adjusting the structural parameters.

The 2D S-T PCs with topological trivial and nontrivial states sharing a common band gap are designed by selecting corresponding structural parameters from Fig. 3 and the band structures of these 2D S-T PCs are calculated as shown in Fig. 4.

As  $d_2/d_1$  goes through values that are less than, equal to, and greater than 1, the band at the Dirac degenerate point

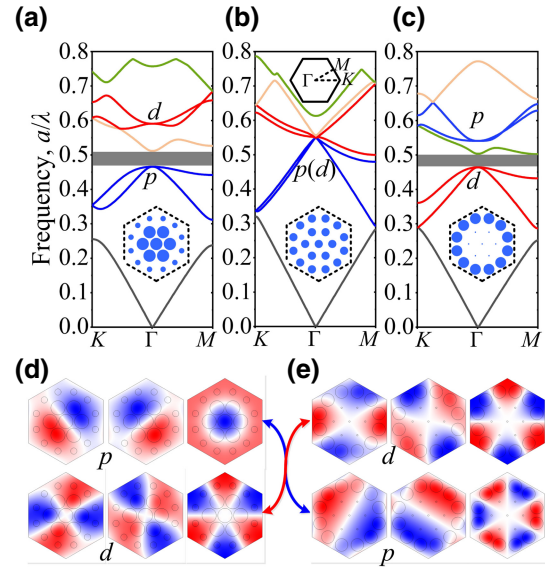


FIG. 4. The band structures of 2D S-T PCs with different structural parameters and the Brillouin zone and its high-symmetry points  $K$ ,  $\Gamma$ , and  $M$ : (a)  $d_1 = 0.9R$ ,  $d_2 = 0.4R$ ,  $d_2/d_1 < 1$ ; (b)  $d_1 = 0.6R$ ,  $d_2 = 0.6R$ ,  $d_2/d_1 = 1$ ; (c)  $d_1 = 0.1R$ ,  $d_2 = 0.8R$ ,  $d_2/d_1 > 1$ . The electric fields at the  $\Gamma$  point from the second to the sixth bands, corresponding to the bands in (d) Fig. 4(a) and (e) Fig. 4(c).  $K$  and  $M$  are the high-symmetry points in the Brillouin zone.

correspondingly goes through open [Fig. 4(a)], degenerate, [Fig. 4(b)] and reopened [Fig. 4(c)] states, accompanied by the inversion of the upper and lower bands at the degenerate point. The band inversion can be reflected from electric field diagrams at the high-symmetry point  $\Gamma$ , as shown in Figs. 4(d) and 4(e). The second and third bands in Fig. 4(a) correspond to the electric field distribution labeled  $p$ , as shown in Fig. 4(d), indicating the  $p$  band. The fifth and sixth bands in Fig. 4(a) correspond to the electric field distribution labeled  $d$ , as shown in Fig. 4(d), indicating the  $d$  band. When the Dirac point goes through the open, degenerate, and reopened process, the corresponding electric field at the  $\Gamma$  point changes as shown in Fig. 4(e). The second and third bands in Fig. 4(c) become the  $d$  band and the fifth and sixth bands in Fig. 4(c) become the  $p$  band. Therefore, when  $d_2/d_1$  goes through values that are less than, equal to, and greater than 1, the band of the system realizes  $p$ - $d$  parity inversion, indicating that the system realizes the PQSHE.

In order to further prove the realization of the PQSHE, the projected band structure of the 2D S-T PC along the  $k_x$  direction and its electric field diagram, as well as the one-way propagation diagram of the U-shaped 2D S-T PC waveguide are calculated, as shown in Fig. 5.

As can be seen from Figs. 4(a) and 4(c), the 2D S-T PC with  $d_1 = 0.9R$  and  $d_2 = 0.4R$  for the topological trivial state and the 2D S-T PC with  $d_1 = 0.1R$  and  $d_2 = 0.8R$  for a topological nontrivial state share a common band

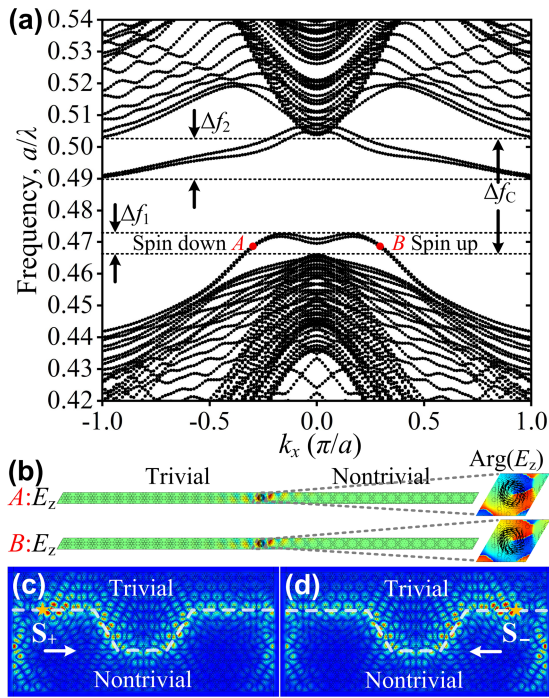


FIG. 5. The projected band structure and topological edge states. (a) The projected band structure of a ribbon-shaped supercell structure consisting of 16 unit cells with  $d_1 = 0.9R$  and  $d_2 = 0.4R$  for the topological trivial state and 16 unit cells with  $d_1 = 0.1R$  and  $d_2 = 0.8R$  for the topological nontrivial state. (b) The electric field and the partial enlarged phase of  $E_z$  corresponding to points  $A$  and  $B$  in the projected band with  $k_x = \pm 0.3(\pi/a)$ . The propagation in the U-shaped waveguide between the 2D S-T PCs with topological trivial and nontrivial states at 140.5 THz [i.e.,  $0.4683(a/\lambda)$ ]: (c)  $S_+$ ; (d)  $S_-$ .

gap. The dispersion relation of the topological edge state can be seen near frequencies  $0.47(a/\lambda)$  and  $0.50(a/\lambda)$  in Fig. 5(a). The frequency widths for generating topological edge states are  $\Delta f_1 = 0.0065(a/\lambda)$  and  $\Delta f_2 = 0.0119(a/\lambda)$ , with the frequency ranging from  $0.4657(a/\lambda)$  to  $0.4722(a/\lambda)$  and from  $0.4911(a/\lambda)$  to  $0.5030(a/\lambda)$ , respectively. The frequency width of the common band gap of the two 2D S-T PCs  $\Delta f_c = 0.0373(a/\lambda)$ , with the frequency ranging from  $0.4657(a/\lambda)$  to  $0.5030(a/\lambda)$ . The ratio  $(\Delta f_1 + \Delta f_2)/\Delta f_c$  is 0.4933, which is smaller than the 0.6885 estimated in Ref. [24]. There is an obvious band gap with the frequency ranging from  $0.4722(a/\lambda)$  to  $0.4911(a/\lambda)$  between the edge bands because the different structure of the topological trivial and nontrivial states destroys the  $C_6$  symmetry, which protects the double degenerate point for the  $p$  and  $d$  bands at the  $\Gamma$  point [24]. As shown in Fig. 5(b), the electric fields  $E_z$  at selected points  $A$  and  $B$  are exactly the same: the phase diagram of  $E_z$  at point  $A$  is clockwise, which represents spin down, while the phase diagram of  $E_z$  at point  $B$  is anticlockwise, which represents spin up. Light source  $S_{\pm} = H_0 e^{i\omega t} (\mathbf{e}_x \mp i\mathbf{e}_y)$  (where  $\mathbf{e}_x$  and  $\mathbf{e}_y$  are the unit vectors along the  $x$  and

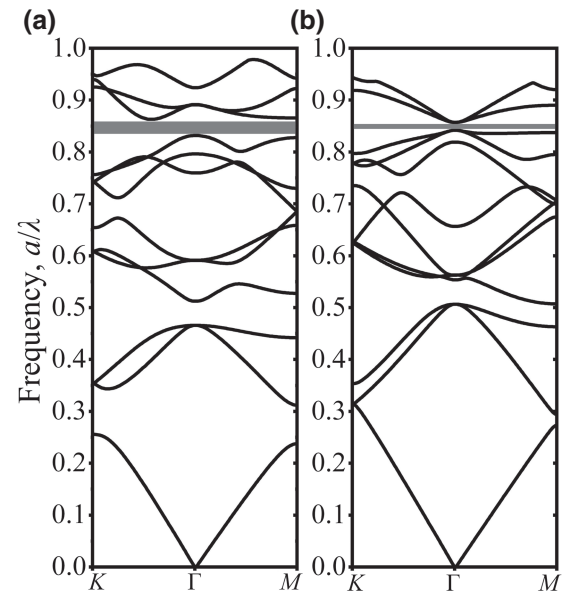


FIG. 6. The band structures of the 2D S-T PCs with different structural parameters: (a)  $d_1 = 0.9R$ ,  $d_2 = 0.4R$ ,  $d_2/d_1 < 1$ ; (b)  $d_1 = 0.4R$ ,  $d_2 = 0.7R$ ,  $d_2/d_1 > 1$ .

$y$  directions) corresponds to the spin up ( $S_+$ ) and spin down ( $S_-$ ) modes, respectively. When the incident light frequency is 140.5 THz [i.e.,  $0.4683(a/\lambda)$ ] and the lattice constant  $a = 1 \mu\text{m}$ , the U-shaped 2D S-T PC waveguide with light source  $S_+$  and  $S_-$  can achieve rightward and leftward one-way propagations, respectively, as shown in Figs. 5(c) and 5(d). The stable propagation of electromagnetic waves in the U-shaped waveguide proves the realization of the PQSHE and topological edge state in the 2D S-T PC.

When the diameter of the cylinders of the topological nontrivial state are adjusted, the common band gap can be found near frequency  $0.85(a/\lambda)$  in 2D S-T PCs with  $d_1 = 0.9R$ ,  $d_2 = 0.4R$  for a topological trivial state and 2D S-T PCs with  $d_1 = 0.4R$ ,  $d_2 = 0.7R$  for a topological nontrivial state, as shown in Figs. 6(a) and 6(b).

In order to further explore whether there is a topological edge state near frequency  $0.85(a/\lambda)$ , the projected band structure of the 2D S-T PC along the  $k_x$  direction and its electric field diagram, as well as the one-way propagation diagram of the U-shaped 2D S-T PC waveguide are calculated, as shown in Fig. 7.

The dispersion relation of the topological edge states can be seen near a frequency of  $0.85(a/\lambda)$  at the projected band structure, as shown in Fig. 7(a). The frequency width for generating topological edge states is  $0.0159(a/\lambda)$ , with the frequency ranging from  $0.8419(a/\lambda)$  to  $0.8578(a/\lambda)$ , which fills the entire common band gap for the two 2D S-T PCs, and there is no band gap between the edge bands. The electric field distributions at points  $A'$  and  $B'$  are strongest at the interfaces and attenuate into the bulk as shown in

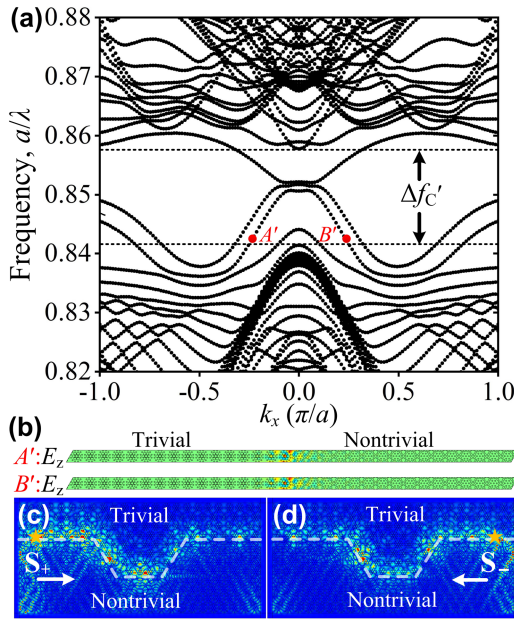


FIG. 7. The high-frequency topological edge state. (a) The projected band structure of a ribbon-shaped supercell structure consisting of 16 unit cells with  $d_1 = 0.9R$  and  $d_2 = 0.4R$  for a topological trivial state and 16 unit cells with  $d_1 = 0.4R$  and  $d_2 = 0.7R$  for a topological nontrivial state. (b) The electric field corresponding to  $A'$  and  $B'$  points in the projected band with  $k_x = \pm 0.24(\pi/a)$ . The propagation in the U-shaped waveguide between 2D S-T PCs with topological trivial and nontrivial states at 252.6 THz [i.e.,  $0.8420(a/\lambda)$ ]: (c)  $S_+$ ; (d)  $S_-$ .

Fig. 7(b), corresponding to the appearance of the topological edge state. The one-way propagations are also realized at 252.6 THz [i.e.,  $0.8420(a/\lambda)$ ], as shown in Figs. 7(c) and 7(d). The stable propagation of electromagnetic waves in the U-shaped waveguide further proves the realization of topological edge state in the 2D S-T PC at a higher frequency. The high-frequency topological edge state can be realized only by adjusting the diameters of the cylinders in the 2D S-T PC for the topological nontrivial state, which further expands the frequency range of the topological edge states.

The topological edge state in the 2D S-T PC can be applied to optical devices such as one-way waveguides [8–12,23–29], splitters [11], optical sensors [27], and optical switchers [44]. In particular, the transmission path and direction of the one-way waveguide can be adjusted by changing just the diameters of the cylinders to realize integrated circuits such as logic-gate devices. This provides a possibility for the realization of programmable photonic topological insulators, a new concept introduced in the acoustic system recently [45], which can be used to realize reconfigurable and programmable optical devices and may lead to important advances in integrated circuits and quantum computation.

## IV. CONCLUSIONS

In this paper, a topological edge state is realized based on the structure arranged using the basic structural unit of the Stampfli-type PQC periodically. The relationship between the diameter ratio  $d_2/d_1$  and the topological trivial or nontrivial state generated in the 2D S-T PC is inferred, i.e., when  $d_2/d_1 < 1$  and  $\omega_{pd} > 0$ , the structure can generate topological trivial states and when  $d_2/d_1 > 1$  and  $\omega_{pd} < 0$ , the structure can generate topological nontrivial states. Finally, the topological edge state and one-way propagation are realized based on 2D S-T PCs with topological trivial and nontrivial states that can realize band inversion and that share a common band gap. The frequency of the topological edge state can be controlled by changing the diameters of the cylinders in the 2D S-T PC, which increases the adjustability and application ranges of the topological edge state. This adjustability will create opportunities for the realization of programmable photonic topological insulators.

## ACKNOWLEDGMENTS

This work was supported by the National Natural Science Foundation of China (Grant No. 61405058), the Natural Science Foundation of Hunan Province (Grant No. 2017JJ2048), and the Fundamental Research Funds for the Central Universities (Grant No. 531118040112). The authors acknowledge Professor Jian-Qiang Liu for software sponsorship. The authors acknowledge Professor Shuang Zhang and Dr. Wen-Long Gao for very helpful discussions.

- [1] S. Raghu and F. D. M. Haldane, Analogs of quantum-Hall-effect edge states in photonic crystals, *Phys. Rev. A* **78**, 033834 (2008).
- [2] F. D. M. Haldane and S. Raghu, Possible Realization of Directional Optical Waveguides in Photonic Crystals with Broken Time-Reversal Symmetry, *Phys. Rev. Lett.* **100**, 013904 (2008).
- [3] L. Lu, J. D. Joannopoulos, and M. Soljačić, Topological photonics, *Nat. Photon.* **8**, 821 (2014).
- [4] X.-C. Sun, C. He, X.-P. Liu, M.-H. Lu, S.-N. Zhu, and Y.-F. Chen, Two-dimensional topological photonic systems, *Prog. Quant. Electron.* **55**, 52 (2017).
- [5] Y. Wu, C. Li, X. Hu, Y. Ao, Y. Zhao, and Q. Gong, Applications of topological photonics in integrated photonic devices, *Adv. Opt. Mater.* **5**, 1700357 (2017).
- [6] A. B. Khanikaev and G. Shvets, Two-dimensional topological photonics, *Nat. Photon.* **11**, 763 (2017).
- [7] T. Ozawa, H. M. Price, A. Amo, N. Goldman, M. Hafezi, L. Lu, M. C. Rechtsman, D. Schuster, J. Simon, O. Zilberberg, and I. Carusotto, Topological photonics, *Rev. Mod. Phys.* **91**, 015006 (2019).

- [8] Z. Wang, Y. D. Chong, J. D. Joannopoulos, and M. Soljačić, Reflection-Free One-Way Edge Modes in a Gyromagnetic Photonic Crystal, *Phys. Rev. Lett.* **100**, 013905 (2008).
- [9] Z. Wang, Y. Chong, J. D. Joannopoulos, and M. Soljačić, Observation of unidirectional backscattering-immune topological electromagnetic states, *Nature* **461**, 772 (2009).
- [10] Y. Poo, R.-X. Wu, Z. Lin, Y. Yang, and C. T. Chan, Experimental Realization of Self-Guiding Unidirectional Electromagnetic Edge States, *Phys. Rev. Lett.* **106**, 093903 (2011).
- [11] S. A. Skirlo, L. Lu, and M. Soljačić, Multimode One-Way Waveguides of Large Chern Numbers, *Phys. Rev. Lett.* **113**, 113904 (2014).
- [12] S. A. Skirlo, L. Lu, Y. Igarashi, Q. Yan, J. Joannopoulos, and M. Soljačić, Experimental Observation of Large Chern Numbers in Photonic Crystals, *Phys. Rev. Lett.* **115**, 253901 (2015).
- [13] L. Lu, C. Fang, L. Fu, S. G. Johnson, J. D. Joannopoulos, and M. Soljačić, Symmetry-protected topological photonic crystal in three dimensions, *Nat. Phys.* **12**, 337 (2016).
- [14] K. Fang, Z. Yu, and S. Fan, Photonic Aharonov-Bohm Effect Based on Dynamic Modulation, *Phys. Rev. Lett.* **108**, 153901 (2012).
- [15] K. Fang, Z. Yu, and S. Fan, Realizing effective magnetic field for photons by controlling the phase of dynamic modulation, *Nat. Photon.* **6**, 782 (2012).
- [16] M. C. Rechtsman, J. M. Zeuner, Y. Plotnik, Y. Lumer, M. Segev, and A. Szameit, Photonic Floquet topological insulators, *Nature* **496**, 196 (2013).
- [17] Y. Zhang, Z. Wu, M. R. Belić, H. Zheng, Z. Wang, M. Xiao, and Y. Zhang, Photonic Floquet topological insulators in atomic ensembles, *Laser Photonics Rev.* **9**, 331 (2015).
- [18] D. Leykam, M. C. Rechtsman, and Y. D. Chong, Anomalous Topological Phases and Unpaired Dirac Cones in Photonic Floquet Topological Insulators, *Phys. Rev. Lett.* **117**, 013902 (2016).
- [19] T. Ma and G. Shvets, All-Si valley-Hall photonic topological insulator, *New J. Phys.* **18**, 025012 (2016).
- [20] J.-W. Dong, X.-D. Chen, H. Zhu, Y. Wang, and X. Zhang, Valley photonic crystals for control of spin and topology, *Nat. Mater.* **16**, 298 (2016).
- [21] X. Ni, D. Purtseladze, D. A. Smirnova, A. Slobozhanyuk, A. Alù, and A. B. Khanikaev, Spin- and valley-polarized one-way Klein tunneling in photonic topological insulators, *Sci. Adv.* **4**, eaap8802 (2018).
- [22] X.-D. Chen, F.-L. Shi, H. Liu, J.-C. Lu, W.-M. Deng, J.-Y. Dai, Q. Cheng, and J.-W. Dong, Tunable Electromagnetic Flow Control in Valley Photonic Crystal Waveguides, *Phys. Rev. Applied* **10**, 044002 (2018).
- [23] L.-H. Wu and X. Hu, Scheme for Achieving a Topological Photonic Crystal by Using Dielectric Material, *Phys. Rev. Lett.* **114**, 223901 (2015).
- [24] L. Xu, H.-X. Wang, Y.-D. Xu, H.-Y. Chen, and J.-H. Jiang, Accidental degeneracy in photonic bands and topological phase transitions in two-dimensional core-shell dielectric photonic crystals, *Opt. Express* **24**, 18059 (2016).
- [25] S. Barik, H. Miyake, W. DeGottardi, E. Waks, and M. Hafezi, Two-dimensionally confined topological edge states in photonic crystals, *New J. Phys.* **18**, 113013 (2016).
- [26] Z. Song, H. Liu, N. Huang, and Z. Wang, Electrically tunable robust edge states in graphene-based topological photonic crystal slabs, *J. Phys. D: Appl. Phys.* **51**, 095108 (2018).
- [27] X. Zhu, H.-X. Wang, C. Xu, Y. Lai, J.-H. Jiang, and S. John, Topological transitions in continuously deformed photonic crystals, *Phys. Rev. B* **97**, 085148 (2018).
- [28] P. Qiu, W. Qiu, J. Ren, Z. Lin, Z. Wang, J.-X. Wang, Q. Kan, and J. Q. Pan, Pseudospin dependent one-way transmission in graphene-based topological plasmonic crystals, *Nanoscale Res. Lett.* **13**, 113 (2018).
- [29] Y. Yang, Y. F. Xu, T. Xu, H.-X. Wang, J.-H. Jiang, X. Hu, and Z. H. Hang, Visualization of a Unidirectional Electromagnetic Waveguide Using Topological Photonic Crystals Made of Dielectric Materials, *Phys. Rev. Lett.* **120**, 217401 (2018).
- [30] M. Oxborrow and C. L. Henley, Random square-triangle tilings: A model for twelvefold-symmetric quasicrystals, *Phys. Rev. B* **48**, 6966 (1993).
- [31] M. E. Zoorob, M. D. B. Charlton, G. J. Parker, J. J. Baumberg, and M. C. Netti, Complete photonic bandgaps in 12-fold symmetric quasicrystals, *Nature* **404**, 740 (2000).
- [32] K. Nozaki and T. Baba, Quasiperiodic photonic crystal microcavity lasers, *Appl. Phys. Lett.* **84**, 4875 (2004).
- [33] S.-P. Chang, K.-P. Sou, C.-H. Chen, Y.-J. Cheng, J.-K. Huang, C.-H. Lin, H.-C. Kuo, C.-Y. Chang, and W.-F. Hsieh, Lasing action in gallium nitride quasicrystal nanorod arrays, *Opt. Express* **20**, 12457 (2012).
- [34] Z. Feng, X. Zhang, Y. Wang, Z.-Y. Li, B. Cheng, and D.-Z. Zhang, Negative Refraction and Imaging Using 12-Fold-Symmetry Quasicrystals, *Phys. Rev. Lett.* **94**, 247402 (2005).
- [35] E. Di Gennaro, C. Miletto, S. Savo, A. Andreone, D. Morello, V. Galdi, G. Castaldi, and V. Pierro, Evidence of local effects in anomalous refraction and focusing properties of dodecagonal photonic quasicrystals, *Phys. Rev. B* **77**, 193104 (2008).
- [36] J.-W. Dong, M.-L. Chang, X.-Q. Huang, Z. H. Hang, Z.-C. Zhong, W.-J. Chen, Z.-Y. Huang, and C. T. Chan, Conical Dispersion and Effective Zero Refractive Index in Photonic Quasicrystals, *Phys. Rev. Lett.* **114**, 163901 (2015).
- [37] S. Kim, C.-S. Kee, and J. Lee, Novel optical properties of six-fold symmetric photonic quasicrystal fibers, *Opt. Express* **15**, 13221 (2007).
- [38] S. Chu, K. Nakkeeran, A. M. Abobaker, S. S. Aphale, P. R. Babu, and K. Senthilnathan, Design and analysis of surface-plasmon-resonance-based photonic quasi-crystal fiber biosensor for high-refractive-index liquid analytes, *IEEE J. Sel. Top. Quantum Electron.* **25**, 1 (2019).
- [39] E. Liu, S. Liang, and J. Liu, Double-cladding structure dependence of guiding characteristics in six-fold symmetric photonic quasi-crystal fiber, *Superlattice. Microstruct.* **130**, 61 (2019).
- [40] E. Liu, W. Tan, B. Yan, J. Xie, R. Ge, and J. Liu, Robust transmission of orbital angular momentum mode based on a dual-cladding photonic quasi-crystal fiber, *J. Phys. D: Appl. Phys.* **52**, 325110 (2019).

- 
- [41] M. A. Bandres, M. C. Rechtsman, and M. Segev, Topological Photonic Quasicrystals: Fractal Topological Spectrum and Protected Transport, *Phys. Rev. X* **6**, 011016 (2016).
- [42] B. A. Bernevig, T. L. Hughes, and S.-C. Zhang, Quantum spin Hall effect and topological phase transition in HgTe quantum wells, *Science* **314**, 1757 (2006).
- [43] K. Sakoda, Double Dirac cones in triangular-lattice metamaterials, *Opt. Express* **20**, 9925 (2012).
- [44] D. Leykam and Y. D. Chong, Edge Solitons in Nonlinear-Photonic Topological Insulators, *Phys. Rev. Lett.* **117**, 143901 (2016).
- [45] J.-P. Xia, D. Jia, H.-X. Sun, S.-Q. Yuan, Y. Ge, Q.-R. Si, and X.-J. Liu, Programmable coding acoustic topological insulator, *Adv. Mater.* **30**, 1805002 (2018).